

SCHOOL OF MECHANICAL,
INDUSTRIAL & AERONAUTICAL
ENGINEERING



SOLAR TRACKER CONTROL SYSTEM

MECHATRONICS II: MECN4029A PROJECT B ASSIGNMENT

2327736	Rivalani Chaki
2325501	Theo Mathebula
2321362	Silindile Mkhathshwa
1863498	Oscia Kholopha

Students must acknowledge all use of AI.

1. Disclosure: Editing/refining *grammar, spelling, formatting*

☒ I acknowledge the use of ChatGPT, V3 to improve the grammar of certain paragraph that I generated myself. I entered the following prompts on 19, 05, 2024:

Original prompt: "Please Highlight grammar error from my provided paragraph"

Follow-up prompt: "Please assist with the ppossible fix for the gramma error"

The output from these prompts was used to state what action was made using the output.

2. Disclosure: Generated/manipulated *code* – list each occurrence

☒ I acknowledge the use of chatgpt, version, Month, Year (chatgpt.com) to troubleshoot a wrong code I generated myself but was giving me an error. I entered the following prompt on 16, 05, 2024:

"The below code give me an error, please fix the code"

☒ ***I declare that the disclosure is complete and truthful.***

Student number: 2327736 |
2325501
2321362
1863498
Course code: MECN4029A
Date: 20/05/2024

EXECUTIVE SUMMARY

This project was undertaken to fully develop a control system that will track the sun's position to increase the amount of irradiance captured as opposed to stationary solar panels that may not be able to capture the maximum amount of irradiance they should. The study was undertaken in the Disteneng area in Polokwane. The nonlinear and linear equations of the system were developed using SIMULINK, and the plots of the responses to different input signals were done to observe the nature of the stability of the system. It was found that the system is inherently and absolutely stable due to its response to disturbances because it quickly reached steady state after the disturbance was removed. Upon completion of the design of the uncontrolled system and observing that the settling time of the uncontrolled system when there is a step input is 392 seconds. This was found not to be feasible because after 392 seconds when the system settles, the sun would have moved by a certain amount. The optimal control technique used was PID as it has a balance of lowering maximum overshoot to 13.3% with zero oscillations, the rise time is 0.0289seconds (which indicates a robust system that responds fast) there is zero steady state error, and the system settles after 0.256 seconds. The sun data for both winter and summer was applied on the system, and it fully tracks the sun's position without any steady state errors.

TABLE OF CONTENTS

Table of Contents

EXECUTIVE SUMMARY	i
LIST OF FIGURES	v
LIST OF TABLES	vi
NOMENCLATURE	vii
1 INTRODUCTION	1
1.1 Background Breakdown	1
1.2 Problem Statement	2
2 MODELLING	3
2.1 Physical model.....	3
2.2 Model assumptions.....	4
2.3 Mathematical Modelling.....	4
2.3.1 Armature controlled DC motor mechanism.	4
2.3.2 Non-linear mathematical model	5
2.3.2 Linear mathematical model.....	6
3 PERFORMANCE	9
3.1 Time Domain Analysis.....	9
3.1.1 Input Disturbances	9
3.1.2 Time Responses	10
3.2 Frequency Domain Analysis	12
3.3 Stability Analysis	16
3.3.1 Routh-Hurwitz	16
3.3.2 pole-zero plot.	16
3.3.3 Nyquist criterion	18
3.3.4 Non-Linear Stability	19
3.4 Controller Necessity.....	20
4 CONTROLLER DESIGN.....	21
4.1 Root-locus technique	21

4.2 Controller	23
4.2.1 PROPORTIONAL	25
4.2.2 PI	27
4.2.3 PD	29
4.2.4 PID	30
5. Solar Tracking Summer vs Winter	32
5.1 Summer tracking.....	33
5.2 Winter tracking.....	34
6 CONCLUSION.....	35
APPENDICES	38
Appendix A1: linearization of the mathematical model.	38
Appendix A2: Root locus Analytical:	39

LIST OF FIGURES

Figure 1: Energy Consumption and National Loadshedding Statistics [2, 5]	1
Figure 2: The Disteneng location and the use of static solar [8, 9]	2
Figure 3: A sketch of Model of solar panel mounting system	3
Figure 4: Armature Controlled DC motor [12].	4
Figure 5: Block diagram of the linear system.	7
Figure 6: Block diagram of the linearized armature DC motor.	8
Figure 7: Block diagram of the linearized solar panel.	8
Figure 8: Block diagram of the solar panel system with armature DC motor supplying torque	8
Figure 9: Input signals used to observe the response of the nonlinear and linear system	9
Figure 10: Position vs time graphs of the linear and nonlinear system for (a) Ramp input (b) Sinusoidal input (c) Step input	11
Figure 11: Velocity vs time graphs of the linear and nonlinear system for (a) Ramp input (b) Sinusoidal input (c) Step input	12
Figure 12: Bode plots of transfer function components	14
Figure 13: Bode plot of the overall transfer function	14
Figure 14: Pole-Zero plot of the transfer function	17
Figure 15: Nyquist plot of the system.	18
Figure 16: Impulse voltage signal.	19
Figure 17: (a) Position vs time graph for an impulse response. (b) Velocity vs time graph for an impulse response	20
Figure 18: block diagram of the linear system	21
Figure 19: PID controller Root locus	22
Figure 20: General schematic of the controlled system	23
Figure 21: Uncontrolled system tracking of input signal	25
Figure 22: Systems response with Proportional Controller	26
Figure 23: Systems response with PI controller	28
Figure 24 :Systems response of a PD controlled system	29
Figure 25: Systems Response to PID Controller	31
Figure 26: Block diagram of the controlled system.	32
Figure 27: Simulink block diagram used for importing solar data.	33
Figure 28: Summer solar tracking position vs time graph.	33
Figure 29: Winter solar tracking position vs time graph	34

LIST OF TABLES

Table 1: Armature controlled DC motor Mechanism specifications:.....	5
Table 2: Transfer function coefficients.	7
Table 3: Routh-Hurwitz stability table.....	16
Table 4: Coefficient of the transfer function	16
Table 5: Pole roots of the transfer function.....	17
Table 6: Routh- Hurwitz for the Root Locus.	22
Table 7: Performance specifications [15].....	25
Table 8: Performance parameters of Proportional controlled system vs uncontrolled system	27
Table 9: Performance parameters of a PI controlled system.....	28
Table 10:Performance parameters of a PD controlled system	30
Table 11:Performance parameters of a PID controlled system	31

NOMENCLATURE

Variable	Variable name	Units
l	Length of solar panel	m
w	Width of solar panel	m
d	Thickness of solar panel	m
$\dot{\theta}$	Angular velocity of solar panel	rad/s
J	Inertia of solar panel	$kg.m^2$
K_d	Damping coefficient	Ns/m
K_t	Motor torque constant	$N.m.A^{-1}$
K_f	Back emf constant	$N.m.A^{-1}$
K_g	Gear ratio constant	-
R	Resistance	Ω
e_m	Back emf	V
V	Voltage	V
i	Current	A
θ	Solar panel position	rad
m	Mass of solar panel	kg
T	Torque	$N.m$

1 INTRODUCTION

1.1 Background Breakdown

South Africa is one of the countries that rely on non-renewable sources for power generation. In 2016, 85.7% of the power generated in South Africa resulted from the burning of coal to produce electricity [1]. The energy consumption in the residential sector of South Africa has increased since early 2000s. As a result of this increase, Eskom have ramped up their energy production to meet the growing demand. Consequently, power stations are operating beyond their optimal capacity, leading to more coal being burnt, which is a non-renewable resource, and consequently, more greenhouse gases being released due to the burning of fossil fuels [2].

Load shedding is the policy employed to manage limited capacity. Eskom currently utilizes this method in South Africa in an attempt to reduce energy consumption by industries and residents. This approach also aims to decrease greenhouse gas emissions resulting from the burning of fuel for power generation. Lastly, this strategy is implemented so engineers can address breakdowns in the power station, as these stations were not originally designed to handle the power demands of the current state of the country [3, 4]. Load shedding is categorized by stages, where Stage 1 means power cuts last for 2 hours or 4 hours, occurring up to three times every 4 days, and the highest stage means the power cut lasts for up to 4 hours, happening 12 times over four days. Figure 1a shows the electricity consumption and Figure 1b shows the national load-shedding hours in South Africa as a results of high energy consumption

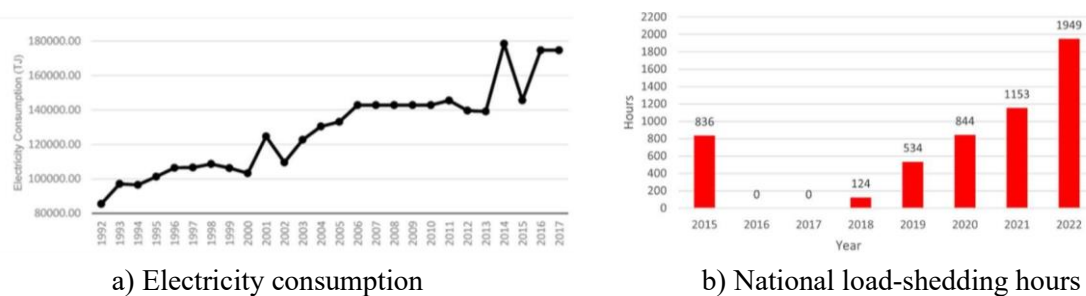


Figure 1: Energy Consumption and National Loadshedding Statistics [2, 5]

Due to load shedding, rural areas like Disteneng, located in Polokwane, Limpopo, face challenges as they lack backup generators to use during outages. Limpopo is one of South Africa's hottest provinces, has recorded temperatures as high as 45.2 degrees Celsius [6]. During load shedding, refrigerators are off, leading to food spoilage due to the high temperatures. Learners also face challenges studying at night due to blackouts. As a result, people are seeking backup systems to use during load shedding.

Solar energy from photovoltaic panels has become an attractive solution for tackling the issues brought by load shedding, especially in regions with abundant sunlight like Limpopo. In places such as Disteneng, where temperatures are high, the installation of static photovoltaic solar panels has gained traction [7]. Despite this, the electricity output from static photovoltaic solar panels method is considered uncompetitive due to its lower efficiency levels. Figure 2a and Figure 2b below shows Disteneng Village and the static photovoltaic solar systems that are currently used.

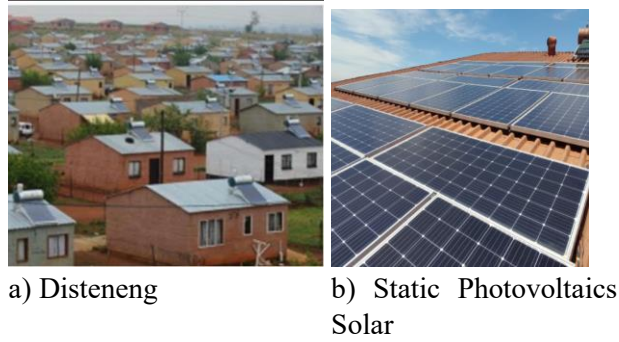


Figure 2: The Disteneng location and the use of static solar [8, 9]

The commonly used solar panel is the 400W solar panel. This is because it is affordable, with prices ranging between R2,000 to R4,000. The 400W panel can also power many electrical appliances, including refrigerators. The specification of 400W solar panel is listed below. The spec of 400W solar panel system

Table 2: Specification of 400W solar panel [10, 11]

Parameters (units)	Value
Rated Maximum Power	400 W
Dimensions (mm)	1722x1134x35
Mechanical load tested (Pa)	2400
Solar Cell	Poly
Weight (kg)	21,9

1.2 Problem Statement

Due to ongoing load shedding in South Africa, up to stage 8, traditional static axis systems are inadequate. A controller for the axis of a solar tracker system is required to optimize solar panel alignment, enhancing energy absorption in Disteneng area.

2 MODELLING

The proposed physical model is a solar system with a mounting system that enables sun tracking to enhance power generation as the sun moves. Figure 3a (side view) and Figure 3b (back view) depicts the schematic representation of the solar tracking mounting system. This model includes the mounting pole to elevate the solar panels, reducing shading from surrounding objects like trees, chimneys, and tall buildings. Additionally, the tracking system include a solar panel base to secure panels against environmental conditions such as wind and rain. The base allows rotation around its centre point, facilitating sun tracking from east to west. This rotation is achieved using a motor, which will be explained in detail.

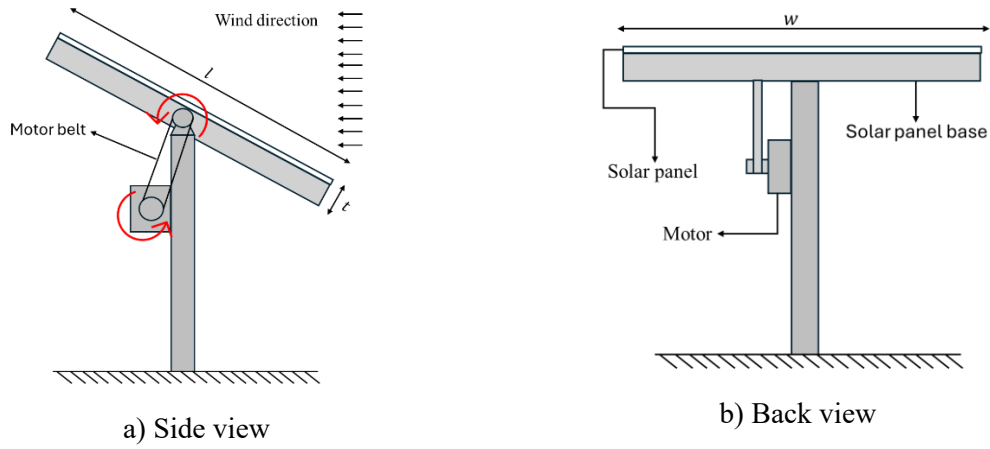
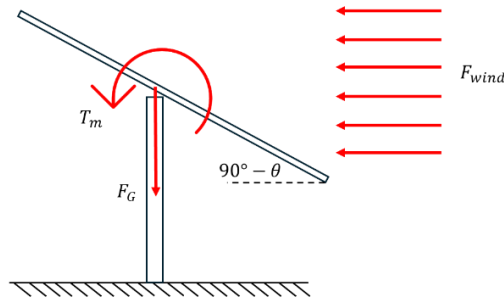


Figure 3: A sketch of Model of solar panel mounting system

2.1 Physical model

Worst Case Scenario

The worst-case scenario for this analysis is when the solar panels are subject to the wind force that is blowing towards the solar in the direction of the rotation of the solar.



The analytical model for the system is essential for understanding the interaction of loads within the system. The free-body diagram used to derive the analytical model of the solar system is shown above.

2.2 Model assumptions

- Constant motor resistance and inductance.
- Motor Torque and emf constants are equal.
- Negligible temperature variation.
- The motor torque and the current have a linear proportionality.
- Moment arm of panel pivot point approximately zero.
- No slipping of the belt.
- Constant damping coefficient.

2.3 Mathematical Modelling

2.3.1 Armature controlled DC motor mechanism.

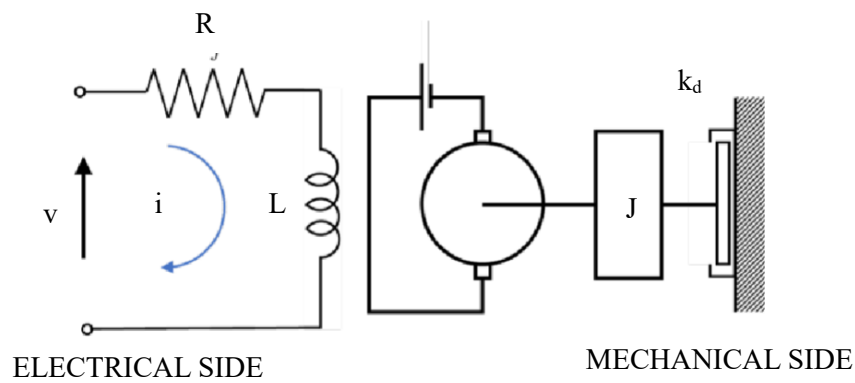


Figure 4: Armature Controlled DC motor [12].

ELECTRICAL SIDE

The voltage input is given by:

$$v = Ri + L \frac{di}{dt} + e_m \quad (1)$$

Where:

$$e_m = k_f \dot{\theta} \quad (2)$$

To account for the gear load, the back emf constant is multiplied by the gear ratio (k_g)

$$e_m = k_g k_f \dot{\theta}$$

Table 1: Armature controlled DC motor Mechanism specifications:

Parameter	Magnitude	Units
k_g	2000	-
k_f	0.05	$N.m.A^{-1}$
k_d	5	Ns/m
k_t	0.05	$N.m.A^{-1}$
L	6	mH
R	3	Ω
V	30	V

MECHANICAL SIDE

Taking sum of torque about the rotating axis

$$J\ddot{\theta} = T - k_d\dot{\theta} - \frac{1}{2}C_D\rho v_\infty^2 lw \cos \theta \quad (3)$$

$$T = k_g k_t i \quad (4)$$

The moment of inertia defined by angle β is given by (ref)

$$J = \frac{1}{12}m(l^2 \cos^2 \beta + d^2 \sin^2 \beta + w^2) \quad (5)$$

Defining the equation (4) by θ :

$$\beta = 90 - \theta \quad (6)$$

$$J = \frac{1}{12}m(l^2 \sin^2 \theta + d^2 \cos^2 \theta + w^2) \quad (7)$$

2.3.2 Non-linear mathematical model

The derivation of the non-linear mathematical model is shown in Appendix A.

$$\frac{1}{12}m(l^2 \cos^2 \beta + d^2 \sin^2 \beta + w^2) \ddot{\theta} = k_g k_t i - k_d \dot{\theta} - \frac{1}{2}C_D\rho v_\infty^2 lw \cos \theta \quad (8)$$

$$\frac{1}{12}m(l^2 \sin^2 \theta + d^2 \cos^2 \theta + w^2) \ddot{\theta} = k_g k_t i - k_d \dot{\theta} - \frac{1}{2}C_D\rho v_\infty^2 lw \cos \theta \quad (9)$$

$$v = Ri + L \frac{di}{dt} + k_g k_f \dot{\theta} \quad (10)$$

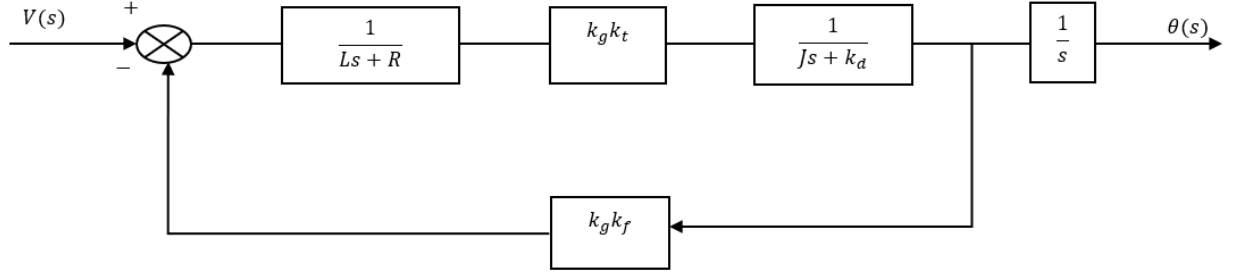


Figure 5: Block diagram of the linear system.

The transfer function of the system is given by:

$$\frac{\theta(s)}{V(s)} = \frac{k_g k_t}{(JL)s^3 + (RJ + k_d L)s^2 + (Rk_d + k_g k_t k_g k_f)s} \quad (16)$$

After simplifications:

$$\frac{\theta(s)}{V(s)} = \frac{1}{\left(\frac{JL}{k_g k_t}\right)s^3 + \left(\frac{RJ + k_d L}{k_g k_t}\right)s^2 + \left(\frac{Rk_d}{k_g k_t} + k_g k_f\right)s} \quad (17)$$

$$\frac{\theta(s)}{V(s)} = \frac{1}{as^3 + bs^2 + cs} \quad (18)$$

Table 2: Transfer function coefficients.

Coefficients	Magnitude
$a = \frac{JL}{k_g k_t}$	0.00014
$b = \frac{RJ + k_d L}{k_g k_t}$	0.07073
$c = \frac{Rk_d}{k_g k_t} + k_g k_f$	100.15

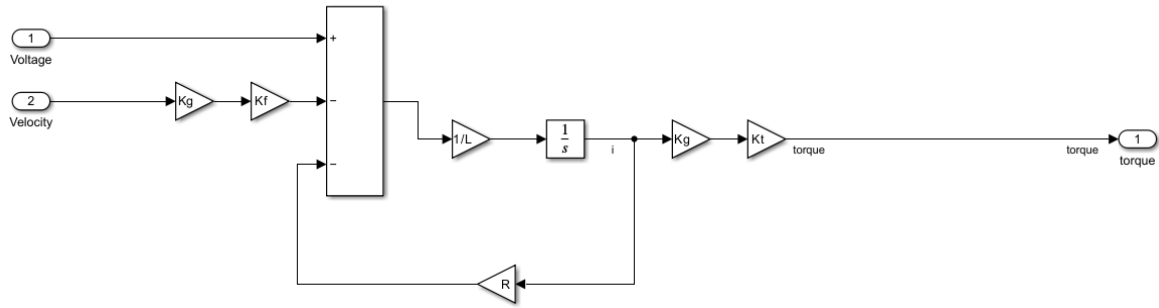


Figure 6:Block diagram of the linearized armature DC motor.

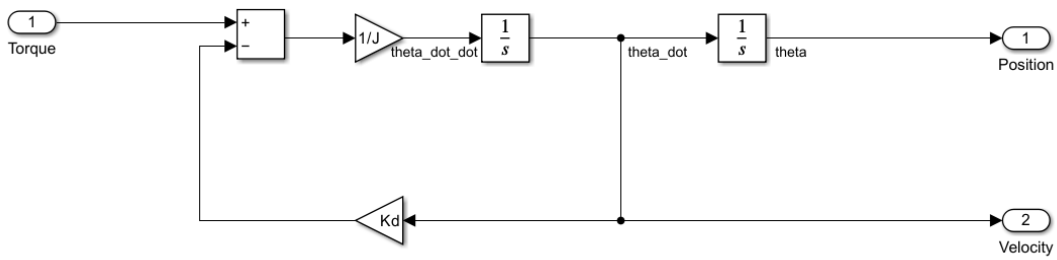


Figure 7:Block diagram of the linearized solar panel.

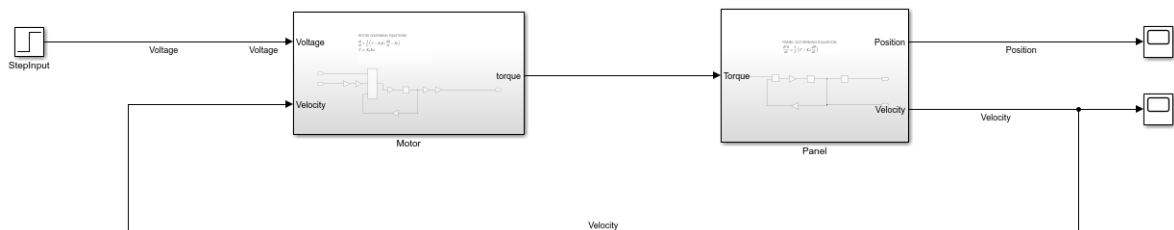


Figure 8:Block diagram of the solar panel system with armature DC motor supplying torque

3 PERFORMANCE

3.1 Time Domain Analysis

3.1.1 Input Disturbances

The realistic input disturbances for a solar tracker that were simulated were Ramp, Step and Sinusoidal voltage input disturbances. This is because the system current input is voltage hence different input signals for the voltage were simulated. The ramp input was chosen because it represents a gradual change in voltage over time which can simulate a gradual increase or decrease in solar irradiance (which could be due to cloud cover or shading).

The sinusoidal input represents the periodic variations in voltage which may be caused by fluctuations in the electrical grid frequency, hence this input allows for assessing the tracking system's performance under cyclic disturbances. The step input represents the sudden or abrupt change in voltage. This simulates sudden changes in sunlight intensity due to passing clouds, this will assess the tracking system's ability to quickly adjust orientation.

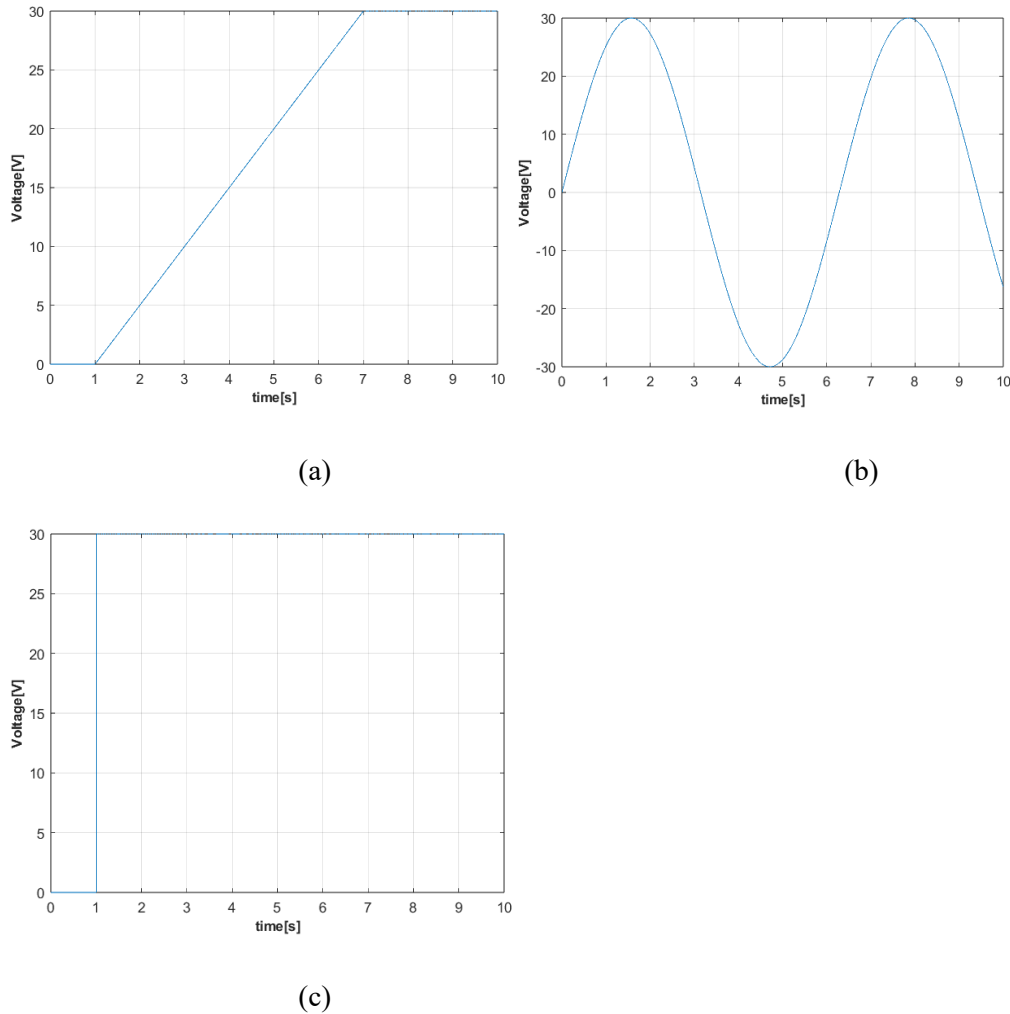


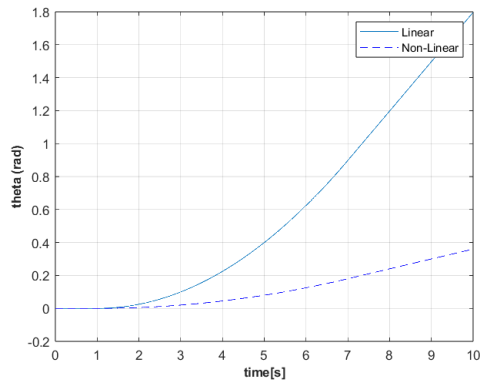
Figure 9: Input signals used to observe the response of the nonlinear and linear system.

3.1.2 Time Responses

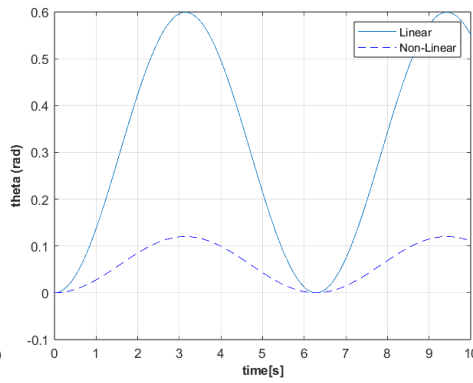
Position

The time responses of the uncontrolled system for both linear and nonlinear were plotted to investigate how the system behaves under different inputs signals as explained in section 3.1.1. For the ramp input, it is observed that the position continues to increase which makes sense because as the voltage increase and the motor shaft rotates, we are expecting the solar panel to also rotate and for a ramp input even after the ramp settles at a voltage of 30V, the voltage is still in the system and will cause the solar panel to move.

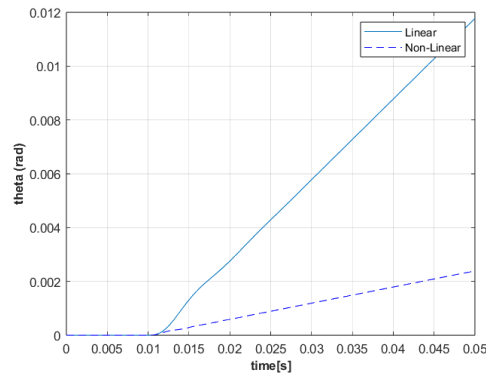
The sinusoidal input shows that both the linear and nonlinear system follow the shape of the input and it is observed that they reach an amplitude of 0.6 radians and 0.1 radians respectively. The differences in the amplitudes will be discussed in the velocity response following up after this section. The response to the step input behaves somewhat similar to the ramp because even after the voltage settles at 30V after the sudden disturbance, the position increases because the voltage is applied to the motor and as per our transfer function the input is voltage and the output is the position (θ), therefore as long as there is voltage in the system, the panel will move.



(a)



(b)



(c)

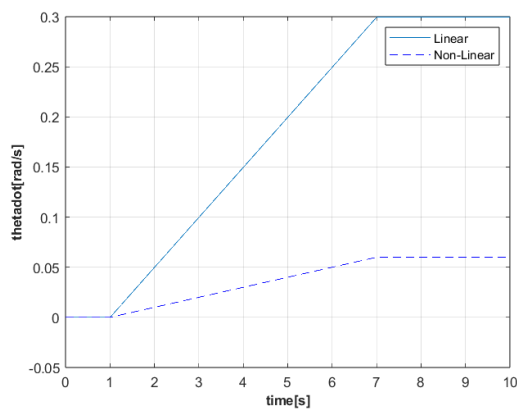
Figure 10: Position vs time graphs of the linear and nonlinear system for (a) Ramp input (b) Sinusoidal input (c) Step input.

Velocity

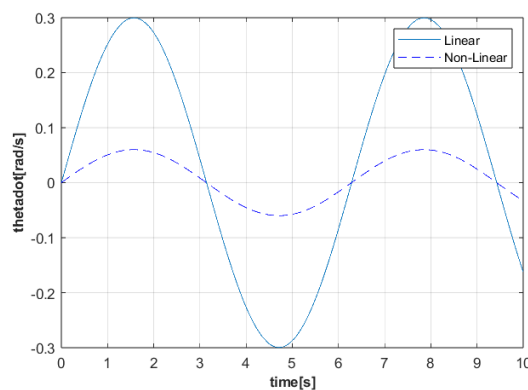
The velocity responses of the uncontrolled linear and non-linear system were plotted to observe the response to the signals mentioned in the sections above. For a ramp input it is seen that as the voltage increases from 0V to 30V, the velocity of the panel also increases (accelerates) and after the voltage has settled the system then rotates at constant speed (no acceleration), the maximum velocity for a ramp input in both the linear and nonlinear system is 0.3 and 0.06 rad/s respectively.

The sinusoidal response for both linear and nonlinear is what we expected because the voltage fluctuates continuously hence, we are expecting the voltage to also fluctuate, and it is seen that the maximum velocity for linear and nonlinear is 0.3 and 0.06 rad/s respectively. The step response for both linear and nonlinear shows an oscillatory behaviour as it is seen that when voltage suddenly increases the velocity overshoots and oscillate until it settles down, interestingly both the linear and nonlinear responses oscillate and settle down to 0.3 and 0.06 rad/s exactly as the ramp and sinusoidal response. This further indicates that our system is stable and reach steady state.

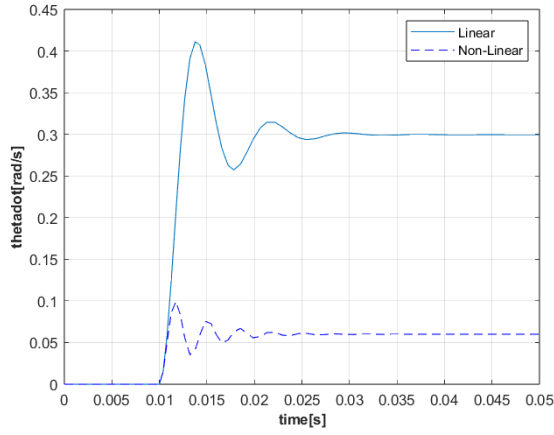
The nonlinear and linear system have the same response in terms of the shape of the functions or the graphs, however they have different amplitudes or maximums. This is because when we linearised, the inertia became constant since we looked at small derivations from initial conditions. This results in neglecting the nonlinear effects because in the nonlinear system, the inertia is not constant, it changes as the panel angle changes. This results in the linear system overestimating the response amplitudes compared to the more accurate nonlinear model.



(a)



(b)



(c)

Figure 11: Velocity vs time graphs of the linear and nonlinear system for (a) Ramp input (b) Sinusoidal input (c) Step input.

3.2 Frequency Domain Analysis

Code plots asymptotes approximation.

Transfer function:

$$G(s) = \frac{7.0922 * 10^3}{s(s^2 + 502.9362s + 7.1028 * 10^5)}$$

Analytical expression of the magnitude and phase response:

$$M(w) = \frac{7.0922 * 10^3}{\sqrt{(502.9362w)^2 + (7.1028 * 10^5 - w^3)^2}}$$

$$Phase = \tan^{-1}(0) - \tan^{-1}\left(\frac{7.1028 * 10^5 - w^3}{-502.9362w^2}\right)$$

The above expression can be used to sketch the bode plot, this approach can be verified by using the asymptotes approximation method, which is found to be easier to plot. The bode plot asymptotes approximation of the overall transfer function was plotted using three decomposition components of the transfer function, $G_k(s)$, $G_1(s)$ and $G_2(s)$. An important value of the bode plot is the break frequency (w_d), where the slope of the plot changes. This point represents the change from the low frequency to the high frequency range, and it was calculated to be 842.9447 rad/s.

Approximation for $G_k(s)$:

$$G_k(s) = 7.0922 * 10^3$$

$$G_k(iw) \approx 7.0922 * 10^3$$

$$M \approx 20\log (7.0922 * 10^3) \text{ dB}$$

$$\text{phase} \approx 0^\circ$$

The magnitude for $G_k(s)$ is a constant which is valid for all values of the frequency. The asymptote of the phase is zero degrees, because the tangent (tan) of the $G_k(s)$ is zero.

Approximation for $G_1(s)$:

$$G_1(s) = \frac{1}{s}$$

$$G_1(iw) \approx \frac{1}{iw}$$

$$M \approx -20\log (w) \quad (-20\text{dB/decade})$$

$$\text{phase} \approx -90^\circ/\text{decade}$$

The magnitude of $G_1(s)$ has a negative slope of -20dB per decades for all values of the frequency, the logarithm of decades (10^n) is n, therefore the magnitude value will decrease by 20n. The phase of this transfer function has a slope which decreases by 90° per decade for all value of the frequency. This is because the tangent term is undefined at $n90^\circ$.

Approximation for $G_2(s)$:

$$G_2(s) = \frac{1}{s^2 + 502.9362s + 7.1028 * 10^5}$$

$$G_2(iw) = \frac{1}{(iw)^2 + 502.9362(iw) + 7.1028 * 10^5}$$

At low frequency:

$$G_2(iw) \approx 7.1028 * 10^{-5}$$

$$M \approx 20\log (7.1028 * 10^{-5}) \text{ dB}$$

$$\text{Phase} \approx 0^\circ$$

At high frequency:

$$G_2(iw) \approx -w^{-2}$$

$$M \approx -40\log (w) \quad (-40 \text{ dB/decade})$$

$$\text{Phase} \approx -180^\circ$$

Intermediate frequency range:

For $\frac{w_d}{10} < \text{frequency} < 10w_d$:

$\text{Phase} \approx -90^\circ/\text{decade}$

The approximation for $G_2(s)$ is done for low frequency, high frequency and the intermediate frequency. At low frequency, the magnitude is low and the phase is a constant of zero degrees. At high frequency, the magnitude decreases with increasing frequency at a rate of -40 dB per decade, and the phase angle approaches negative 180 degrees. In the intermediate frequency range, the phase has a slope of -90° per decade.

Bode plots using Matlab functions.

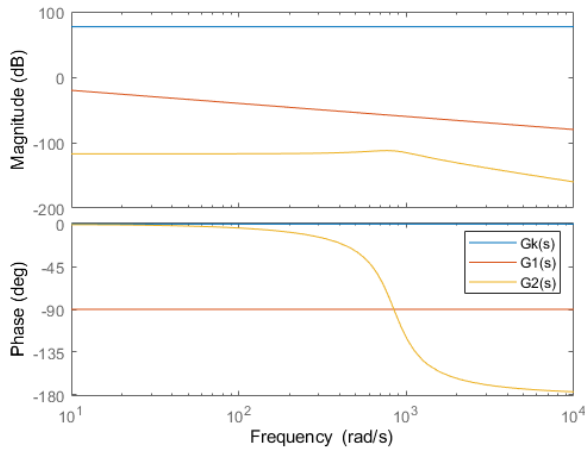


Figure 12: Bode plots of transfer function components

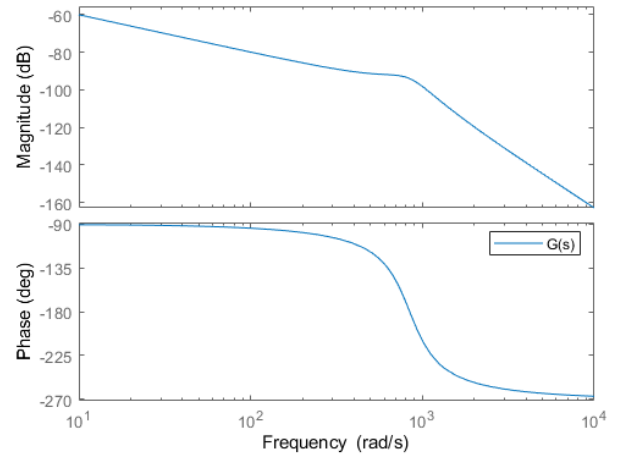


Figure 13: Bode plot of the overall transfer function

The bode of the three components of the transfer function in figure 12 were combined to plot the resultant bode in figure 13. Matlab was used to compute the components and resultant bode plots. The results obtained from the Matlab build in function, match with the asymptotes of the analytical approximations.

The bode plot start with a maximum value of -60db in magnitude and slopes downward at a constant rate (-40dB/decades), when it reaches the break frequency, the slope changes to -80dB per decade. The negative slope of the bode plot indicates the gain decreases with increasing frequency. The rapid change after the breaking frequency suggests a more rapid decrease in gain with increasing frequency. The

phase plot at low frequency has a constant phase of -90° , this low frequency approximation is valid until 10% of the break frequency. The approximation for high frequency is valid from $10\omega_d$, where the phase is -270° . In between the high and low frequency range of the phase plot, the phase has a slope of -90° per decade. The negative phase slope is due to the presence of poles at the origin and complex roots.

The bandwidth of the uncontrolled system was found to be 10 rad/s using Matlab. The bandwidth is the measure of the system's performance at different frequency signals. The bandwidth is the frequency evaluated at the point where the magnitude of the bode plot has decreased by 3 dB from the peak magnitude value. The bandwidth indicates that the system is more efficient in interpreting signals whose frequency range lie near 10 rad/s.

3.3 Stability Analysis

3.3.1 Routh-Hurwitz

The Routh-Hurwitz stability criterion was used to determine the presence of unstable roots if any exist. The characteristic equation is presented below is a 3rd degree polynomial, which is taken from the transfer function, equation (13).

$$as^3 + bs^2 + cs + d = 0$$

$$0.00014s^3 + 0.0773s^2 + 100.15s = 0$$

Table 3: Routh-Hurwitz stability table.

s^3	0.00014	100.15s
s^2	0.0773	0
s^1	100.15	0
s^0	0	

The polynomial has no left column sign changes, and hence, no roots exist in the right half plane. Therefore, this indicates that the system is stable since all roots of the system lie on the left half plane of the s-plane.

3.3.2 pole-zero plot.

This section details the pole-zero plot of the transfer function given in the following format.

$$T(s) = \frac{N(s)}{D(s)} = \frac{1}{as^3 + bs^2 + cs + d}$$

Where the values of a, b, c , and d are the coefficient shown in the table

Table 4: Coefficient of the transfer function

a	b	c	d
0.00014	0.07073	100.15	0

The numerator $N(s)$ of the transfer function is used to find the zeros, since in this case it is constant. It shows there are no frequencies in the s-domain such that the transfer function will be zero hence there are no zeros for the transfer function. Poles are the frequencies at which the transfer function $T(s)$

becomes undefined or infinite. In physical meaning, they represent the stability of the transfer function, $T(s)$. These points are achieved by setting the denominator $D(s)$ of the transfer function $T(s)$ to zero. For the given transfer function.

$$D(s) = aS^3 + bS^2 + cS + d = 0$$

$$0.00014S^3 + 0.0773S^2 + 100.15S = 0$$

$$S(0.00014S^2 + 0.0773S + 100.15) = 0$$

The solution to $D(s) = 0$ were obtained and tabulate below:

Table 5: Pole roots of the transfer function

Root	Value
S_1	0
S_2	$-276.07 + j799.46$
S_3	$-276.07 - j799.46$

Using the S_1, S_2 , and S_3 , the Pole and the Zeros can be plotted now.

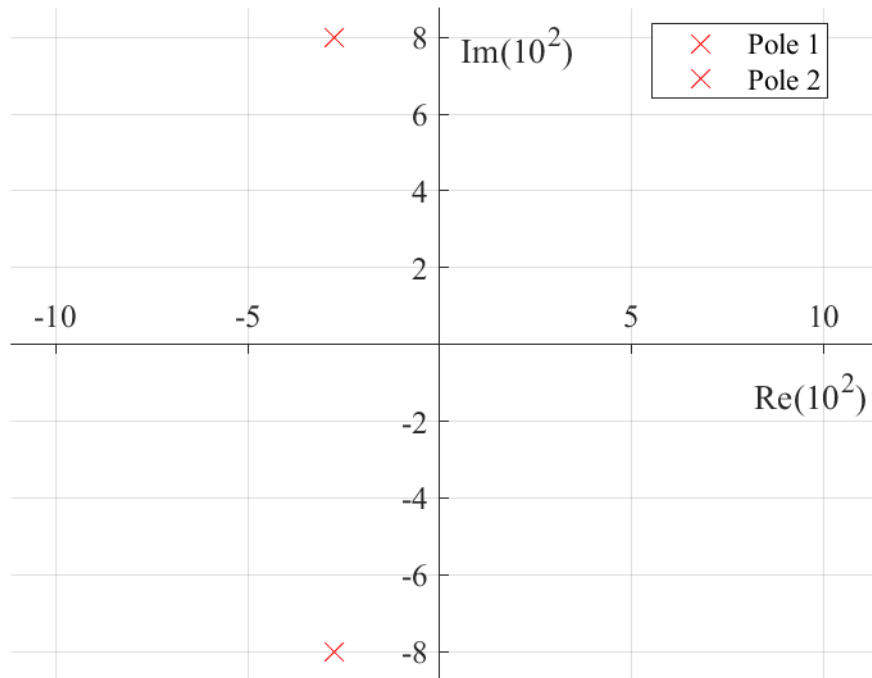


Figure 14: Pole-Zero plot of the transfer function

Figure 14 shows the poles plot. Since the transfer function does not have any zeros, only poles were plotted. Both Pole 1 and Pole 2 are located on the left side of the imaginary axis. This implies that the

system is stable. Stability indicates that the system will be able to settle down to equilibrium after experiencing a disturbance.

3.3.3 Nyquist criterion

The Nyquist plot is one of the important criteria, which is used to determine stability of the system, this plot is found by transforming the transfer function into the real and imaginary axis.

$$G_2(iw) = \frac{7.0922 * 10^3}{(iw)^2 + 502.9362(iw) + 7.1028 * 10^5}$$

The real and imaginary part of the above transfer function:

$$Re = \frac{Aw^2}{Bw^4 + (w^3 + Cw)^2}$$

$$Im = \frac{w^2 + Cw}{Bw^4 + (w^3 + Cw)^2}$$

Where $A = -3.5669 * 10^6$

$B = -502.9363$

$C = -7.1028 * 10^5$

The above real and imaginary equations were evaluated for a range of frequencies (w), and the graph shown below was plotted from these values.

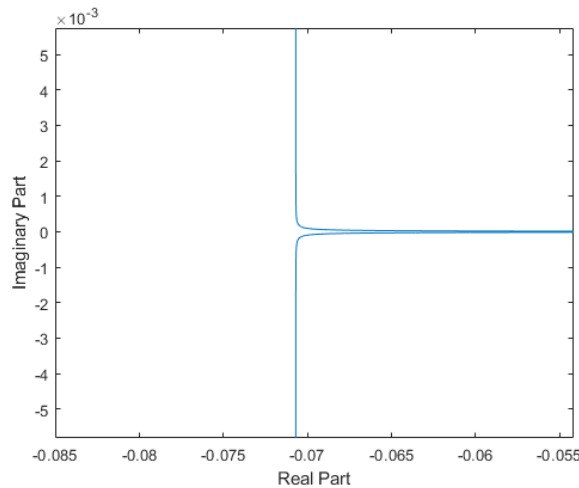


Figure 15: Nyquist plot of the system.

The stability of the system represented by (s) was determined using the Nyquist stability criterion. By examining the Nyquist plot, which depicts the frequency response of the system on the complex plane, it was observed that in figure 15 there were no encirclements of the critical point $(-1, j0)$, indicating $N=0$. Additionally, there were no poles situated in the right half-plane ($p=0$) as shown in the pole-zero plot in figure 14. According to the Nyquist

stability criterion, the system is stable if $z-p-N=0$. As $z=0$, signifying stability, the system is deemed stable. This conclusion holds despite the existence of complex-conjugate poles in the left half-plane, as the absence of encirclements ensures stability irrespective of the presence of such poles. Thus, the Nyquist stability criterion serves as a robust approach for assessing the stability of dynamic systems based on their frequency response characteristics. The Nyquist plot is thin or shrunk, this is because the response gain is relatively high at low frequencies.

3.3.4 Non-Linear Stability

The analytical tools we have for a linearized system cannot be directly used to analyze the stability of a nonlinear system. It is known from theory that a system is absolutely stable if in equilibrium it is momentarily excited by a disturbance input and when the disturbance is removed, the system returns to equilibrium. The key word is “momentarily excited” meaning the disturbance is there for a short period then removed, the signal that could accurately represent this is an “impulse” where we introduced a disturbance for short period to observe how the system responds to the input. The signal is shown in the figure below, where the voltage rises to 30V then drops to 0V.

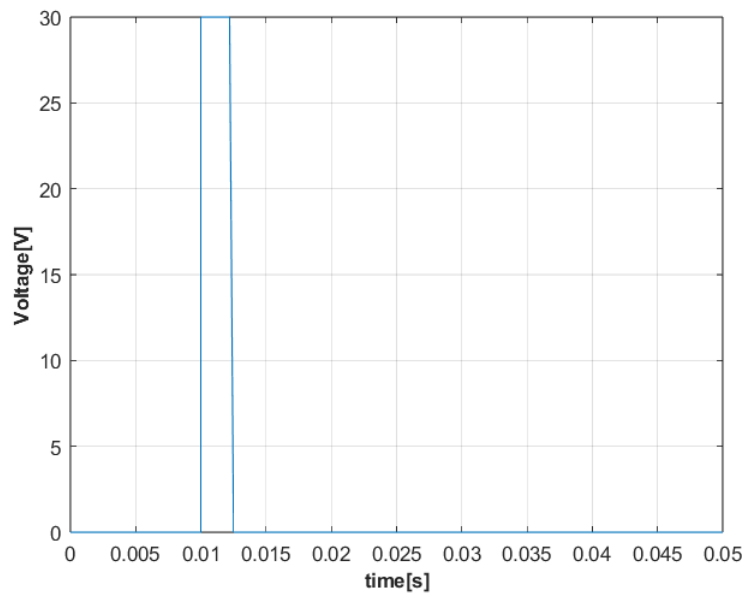


Figure 16: Impulse voltage signal.

The velocity and position of response for the nonlinear system were plotted to observe the behavior of the system under a momentary disturbance. The position plot shows that the position overshoots to 0.00018 radians and oscillates until it returns to a steady state value of 0.00015 radians which is what we expect from a stable system that when a disturbance is introduced it moves but return to a steady state. This is further confirmed by the velocity vs time graph as it shows that when the impulse is introduced, the system overshoots and oscillate but returns to a velocity of 0rad/s and that is what we expect that when the voltage returns to zero the panel should not be moving at all.

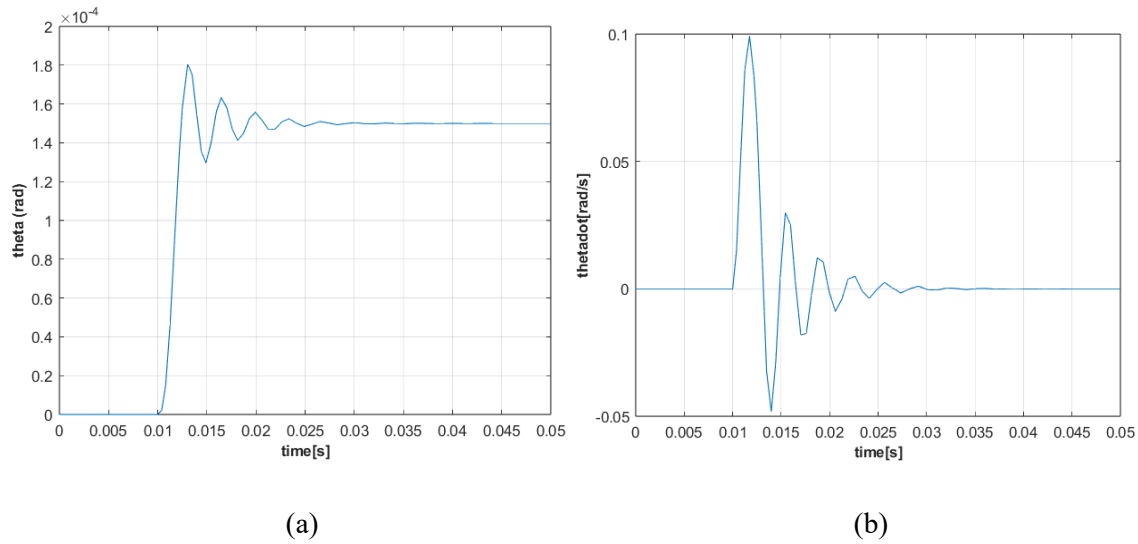


Figure 17: (a) Position vs time graph for an impulse response. (b) Velocity vs time graph for an impulse response

BIBO Analysis

The plots for bounded inputs such as ramp and sinusoidal response were shown earlier, and according to this analysis, the output or the response should be bounded within certain limits. It is observed that the responses to these inputs are also bounded, and this further confirms that our nonlinear system is absolutely stable.

3.4 Controller Necessity

Improved plant design may mitigate the need for complex control strategies in certain cases however it may not completely eliminate the need for control. The system can be designed with fewer linearities such that the system behaviour can be predictable and easier to control i.e in our case we can improve damping which can lead to faster response times, reducing oscillations which will result in reducing the need for sophisticated control techniques. The last point in how this can be achieved is to design a system that is inherently stable without active control, however this does not eliminate the need for control because a system can be stable but not meet the design specifications such as settling time, steady state error etc which may be achieved by means of a controller.

4 CONTROLLER DESIGN

4.1 Root-locus technique

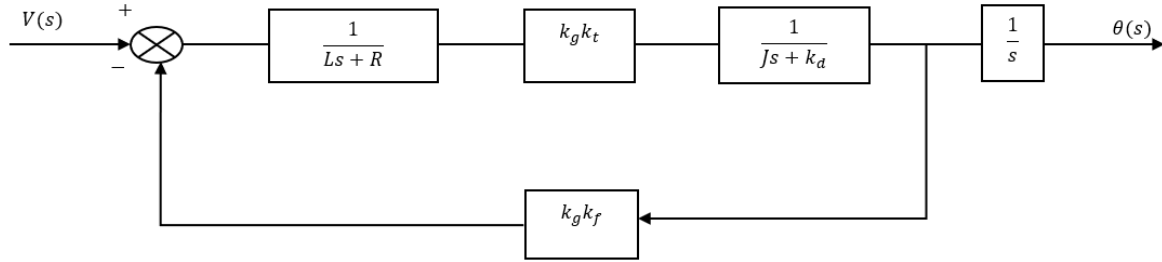


Figure 18: block diagram of the linear system.

From the block diagram represented above, the characteristic equation of the open loop system is shown in the equation below:

$$G(s)H(s) = \frac{1}{0.00014s^3 + 0.070773s^2 + 100.15s} \quad (18)$$

The characteristic equation for the general problem is represented by equation (20):

$$1 + \frac{K}{0.00014s^3 + 0.070773s^2 + 100.15s} = 0 \quad (20)$$

The system has 3 of poles and does not have zeros, i.e., $P=3$ and $Z=0$, respectively. The 3 poles located at $s_1 = 0$ and $s_{2,3} = -252.61 \pm 807.18i$. Therefore, this indicated that there will 3 loci starting at 0 and the other 2 starting at -252.61 ± 807.18 on the root locus. Since there are no zeros, all the loci will tend to infinity along the asymptote. The breakaway and break-in points were found from using $\frac{dK}{ds} = 0$, and the points were calculated to be at $s_{1,2} = -168.45 \pm 458.34i$ on the root locus. The corresponding value of K at the breakaway point was calculated to be ***. The angles that the asymptotes make with the real axis were found to be at $\theta = -60^\circ, 60^\circ$ and -180° . Moreover, the common point of intersection for the three loci were to be at 168.407, and the points at which the loci cross the imaginary axis, and the associated values of k were calculated by substituting $s = i\omega$ into the characteristic equation of K . From which the following were obtained:

$$\omega = 0, K = 0, \quad \text{or,} \quad \omega = 845.154, K = 50627.971.$$

For confirming Routh-Hurwitz was used, and the following was obtained:

Table 6: Routh- Hurwitz for the Root Locus.

s^3	0.00014	100.15
s^2	0.070773	K
s^1	$\frac{7.0879 - 0.00014K}{0.070773}$	0
s^0	K	0

From Routh-Hurwitz criterion, the range of K values were found to be $0 < K < 50627.857$ for the system to be stable.

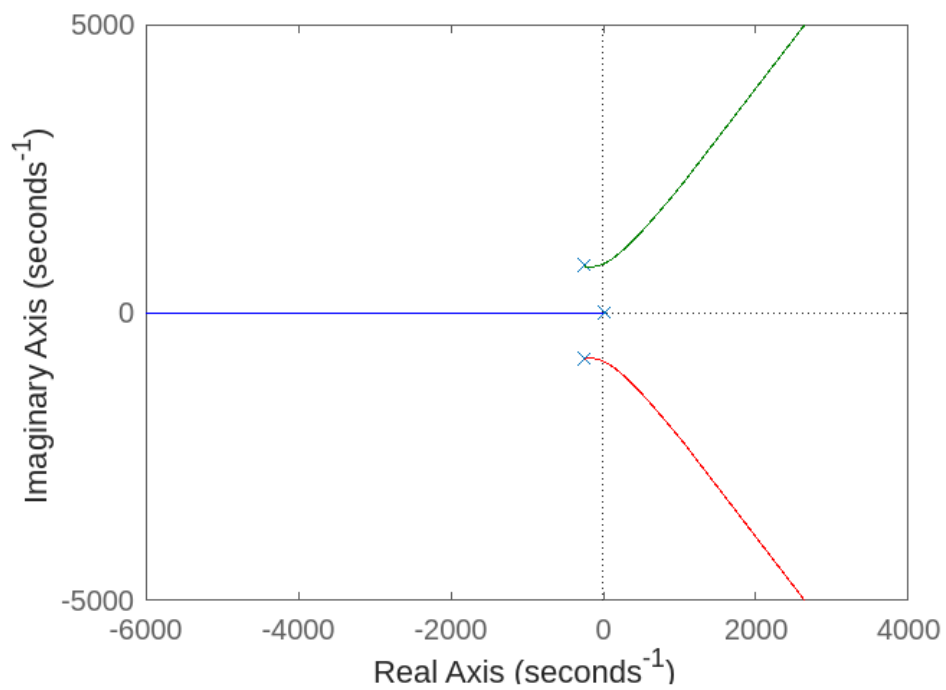


Figure 19: PID controller Root locus

4.2 Controller

The design of the controller aims to help the mechatronic system to achieve the desired performance specifications, i.e stability, overshoot, response time and steady state error. Controller parameters were interpolated until the system's requirement were meant. The controller comprises of three components the proportional, integral, and derivative control. The proportional controller aims to provide an immediate correction to the system such as increasing the speed of the motor, based on the current error. The integral controller ensures zero steady state error by integrating the error over time. The derivative controller reduces the rate of change of the error, which ensures better performance of the system such as stability and overshoot [13].

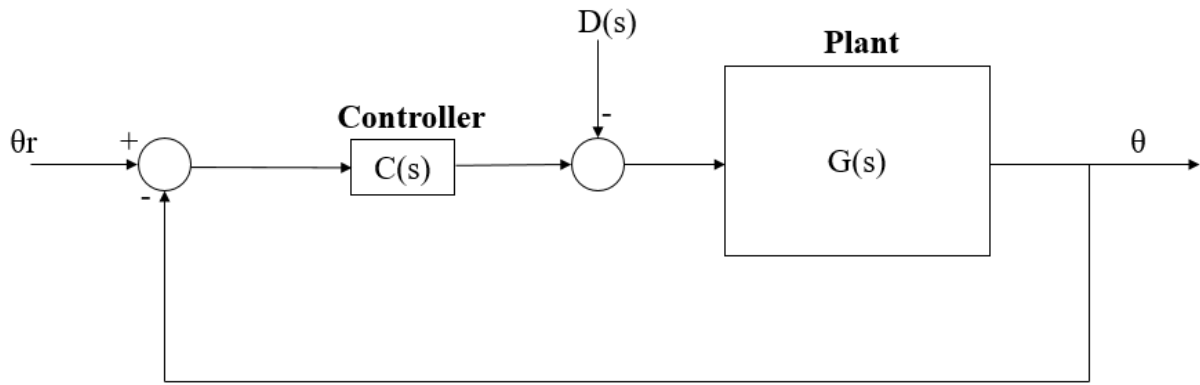


Figure 20: General schematic of the controlled system

For the above system in figure 12, different types of controllers are used, and evaluated based on the system's performance specifications. The steady state final value of the system are evaluated due to the influence of the step reference input and disturbance. These final values are calculated using the final value theorem.

Final value theorem for a step input [14]:

$$\theta_{\text{final}} = \lim_{s \rightarrow 0} s \theta(s)$$

Using Proportional controller (P):

$$C(s) = K_p$$

The feedback transfer function becomes:

$$\frac{\theta(s)}{\theta_r(s)} = \frac{7092.2K_p}{s^3 + 502.9362s^2 + 7.1028 \times 10^5s + 7092.2K_p}$$

$$\frac{\theta(s)}{D(s)} = \frac{7092.2}{s^3 + 502.9362s^2 + 7.1028 \times 10^5s - 7092.2K_p}$$

Final steady state values:

$$\theta_{\text{final}} = 1 \quad (\text{due to reference input})$$

$$\theta_{\text{final}} = -\frac{1}{K} \quad (\text{due to disturbance})$$

The above final values indicates that the proportional controller is able to correctly adjust the system's output to match the desired set value, however it cannot eliminate the influence of the disturbance in the final value. Due to this limitation of the proportional controller, another controller is introduced. The integral and the proportional controller are discussed below, to see the improvement from using the proportional controller only.

Using the proportional and integral controller (PI):

$$C(s) = K_p + \frac{K_I}{s}$$

The feedback transfer function becomes:

$$\frac{\theta(s)}{\theta_r(s)} = \frac{7092.2(K_p + K_I s)}{s^4 + 502.9362s^3 + 7.1028 * 10^5 s^2 + K_p s + 7092.2K_I}$$

$$\frac{\theta(s)}{D(s)} = \frac{7092.2s}{s^4 + 502.9362s^3 + 7.1028 * 10^5 s^2 - K_p s - 7092.2K_I}$$

Final steady state values:

$$\theta_{\text{final}} = 1 \quad (\text{due to reference input})$$

$$\theta_{\text{final}} = 0 \quad (\text{due to disturbance})$$

The PI controller can successfully obtain the output which matches the reference input and can eliminate the steady state error due to the disturbance. This controller can improve steady state performance successfully but does not account for the transient response; a derivation controller must be added to correct this.

Table 7: Performance specifications [15]

Maximum overshoot (M_p) [%]	0.32890 (20%)
Rise time (t_r) [s]	0.16300
Settling time (t_s) [s]	Within 2% of the final value (0.2523)
Steady state error (e_{ss})	0.01256
Gain margin	20 dB
Bandwidth	

The control system design tool was used to determine the values of K for the system will meet the performance specifications presented in table 7.

4.2.1 PROPORTIONAL

The graph below shows that the uncontrolled system takes a long time to reach a steady state value of the input, although it is stable it takes 392 seconds to settle, and the other parameters are shown in the table discussing the parameters of the proportional controller vs the uncontrolled system. Due to our desire for the solar tracker to be robust we would want the system to respond much quicker and this section explores how the proportional control affects the performance of the system.

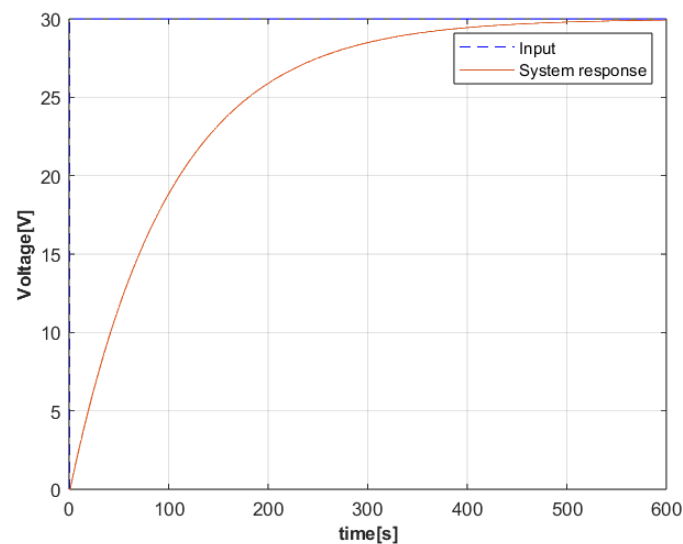


Figure 21: Uncontrolled system tracking of input signal

From the plot below, it is shown that when proportional control is used, there is a huge oscillation before the system reaches steady state. Although at the end the system tracks the input signal, the system overshoots several times before coming to rest, however due to the system itself being inherently stable, surprisingly there is no steady state error when the system finally reaches steady state. The K_p value used that was used through the PID tuner was 37344.3559 which falls within our range of K as determined by the root-locus technique.

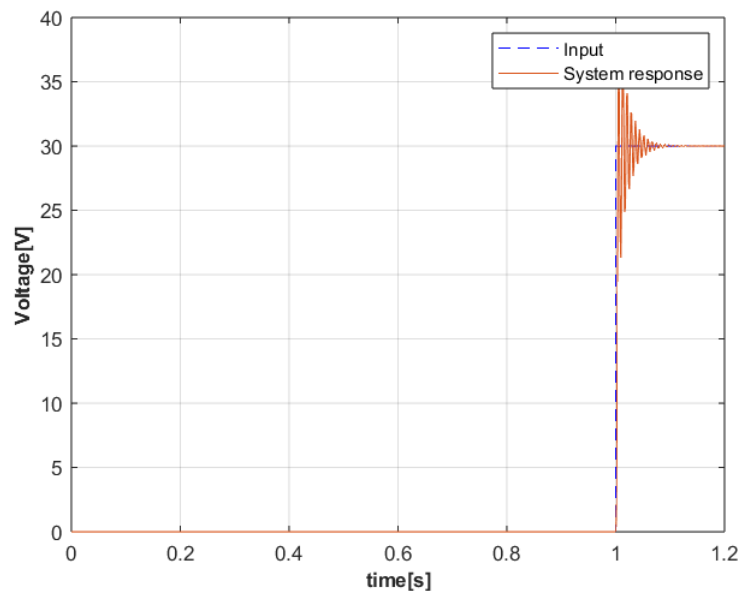


Figure 22: Systems response with Proportional Controller

The performance parameters of the controlled system with a proportional controller are shown below. One thing to note is that there is a huge improvement from the performance of the uncontrolled plant when we use a controller, the settling time without a controller was 392 seconds which decreased to 0.0561 seconds when we introduced the controller.

Table 8: Performance parameters of Proportional controlled system vs uncontrolled system

Controller parameters		
	Tuned	block
P	37344.3559	1
I	n/a	n/a
D	n/a	n/a
N	n/a	n/a
Performance and robustness		
	Tuned	Block
Rise time (t_r) [s]	0.00233	220
Settling time (t_s) [s]	0.0561	392
Maximum overshoot (M_p) [%]	23.5	0
Peak	1.25	0.999
Gain margin	2.58 dB @829 rad/s	94° @ 843 rad/s
Phase margin	60° @ 48 rad/s	90° @ 0.00999 rad/s
Closed-loop stability	stable	Stable

4.2.2 PI

This technique combines the proportional control with integral action to eliminate steady-state error by considering the sum of past errors. It is seen from the plot that this technique eliminates those huge oscillations we saw from proportional control, and thus eliminating those steady-state errors. However, this technique causes huge overshoots which will need more iteration to tune. The iterations performed made us discover that high K_I values reduces steady state error more effectively but may introduce overshoot and slower response of set too high.

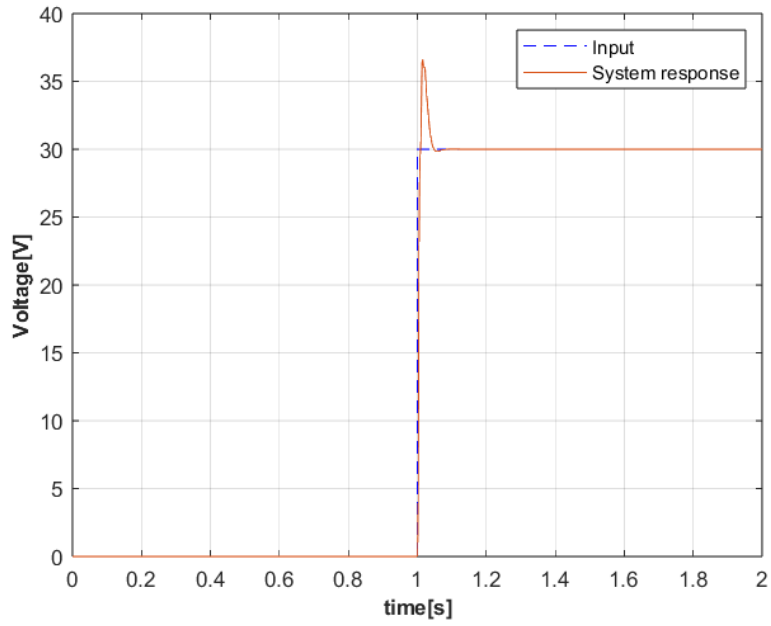


Figure 23: Systems response with PI controller.

The performance parameters of the PI controlled system are summarized in the table below and once thing to note is that the settling time and the maximum overshoot decreased compared to the system with Proportional Control.

Table 9: Performance parameters of a PI controlled system

Controller parameters		
	Tuned	block
P	17364.1451	1
I	1349044.3089	1
D	n/a	n/a
N	n/a	n/a
Performance and robustness		
	Tuned	Block
Rise time (t_r) [s]	0.00421	10.6
Settling time (t_s) [s]	0.0409	760
Maximum overshoot (M_p) [%]	22.4	85.5
Peak	1.22	1.85
Gain margin	8.75 dB @ 819 rad/s	94° @ 843 rad/s
Phase margin	60° @ 194 rad/s	5.72° @ 0.1 rad/s
Closed-loop stability	stable	Stable

4.2.3 PD

This technique combines proportional control with derivative action, which anticipates future error based on its rate of change. The plot shows that this method reduces overshoot and oscillations (compared to proportional control alone) however there are still oscillations compared to PI. It is seen from the plot that high K_D values lead to jittery movements. The tuned response is still stable and does eventually reach steady state.

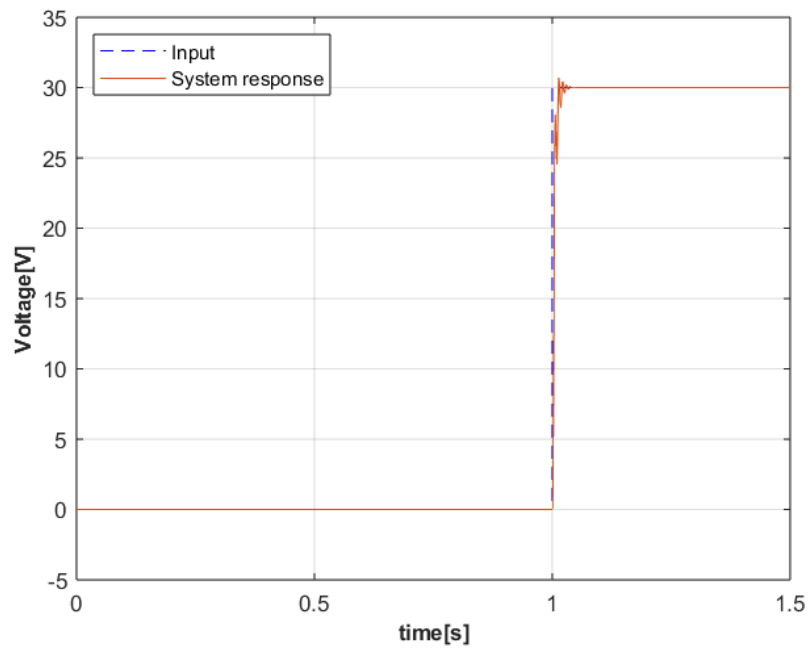


Figure 24 :Systems response of a PD controlled system

As expected, the maximum overshoot is way less compared to the other methods which is due to the derivative action of the PD controller, consequently the settling time is much quicker.

Table 10: Performance parameters of a PD controlled system

Controller parameters		
	Tuned	block
P	23093.905	1
I	n/a	n/a
D	0	0
N	100	100
Performance and robustness		
	Tuned	Block
Rise time (t_r) [s]	0.00377	220
Settling time (t_s) [s]	0.0192	392
Maximum overshoot (M_p) [%]	2.66	0
Peak	1.03	0.999
Gain margin	6.76 dB @ 829 rad/s	94° @ 843 rad/s
Phase margin	79.1° @ 48 rad/s	90° @ 0.00999 rad/s
Closed-loop stability	stable	Stable

4.2.4 PID

The technique itself combines all the three control actions however it presents complexities in tuning since all three control actions must be factored in. From the plot it is seen that this technique has a smooth response, however it does overshoot without oscillations and smoothly comes down to steady state. The response is similar to that of the PI controlled system the differences are in the magnitudes of the gains used for the integral action. When using PI the value of K_I is 1349044.3089 however when using the PID technique it reduces to 45069.518, the maximum overshoots decreases from 22.4% to 13.3%. The tuning app helped us notice that, an increase in P gain increases responsiveness but risks overshoot, increasing I gain eliminates steady state error faster but may slow the response and cause overshoot if it is too high and increasing D gain improves damping which reduces overshoot and oscillations but too high of D gain make the system to have jittery movements.

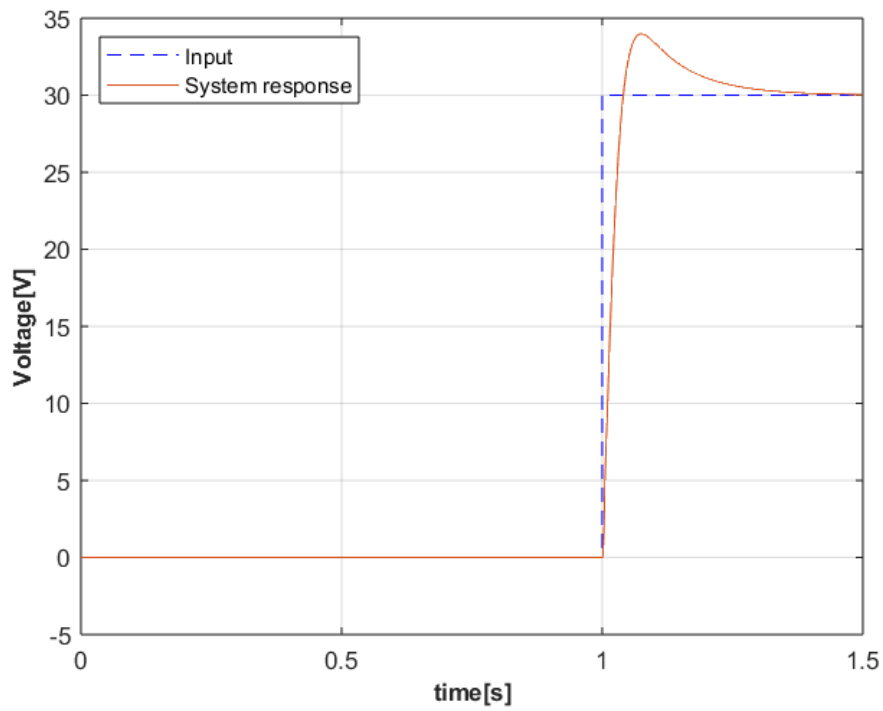


Figure 25: Systems Response to PID Controller

Table 11: Performance parameters of a PID controlled system

Controller parameters		
	Tuned	block
P	4922.7881	23093.9051
I	45069.518	1349044.3089
D	-17.974	0
N	82.9588	100
Performance and robustness		
	Tuned	Block
Maximum overshoot (M_p) [%]	13.3	20.1
Rise time (t_r) [s]	0.0289	0.00319
Settling time (t_s) [s]	0.256	0.0457
Peak	1.13	1.2
Gain margin	22.0 dB @ 829 rad/s	6.39° @ 825 rad/s
Phase margin	69° @ 48 rad/s	65.9° @ 255 rad/s
Closed-loop stability	stable	Stable

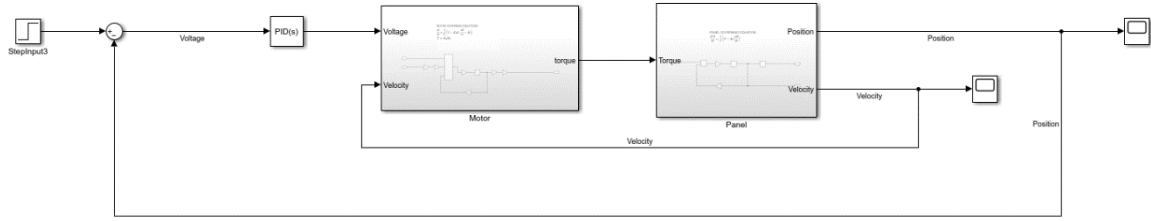
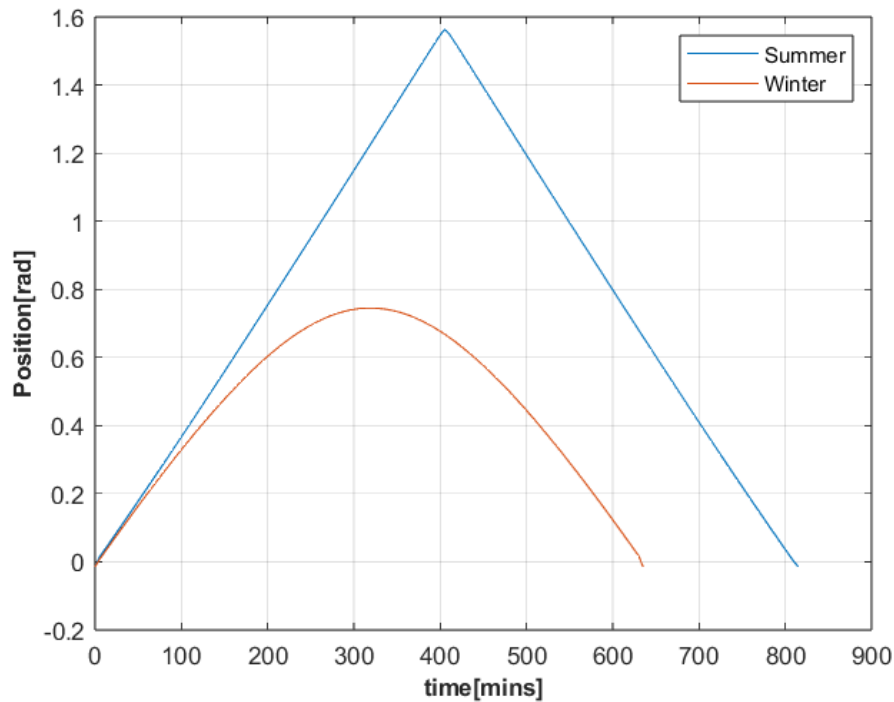


Figure 26: Block diagram of the controlled system.

5. Solar Tracking Summer vs Winter

The solar data was obtained by using sunearthtools [16] and placing the exact coordinates of the place we are tracking the sun from. Data for both winter and summer was extracted by using last year's data for the 20th of June and 21st of December which is the start of winter and summer respectively. The data obtained was used on our solar tracking system with PID controller to observe how it tracks the sun's position since we were doing position control.



The solar data was loaded into MATLAB by using the readable function then imported to Simulink using data import/export under modelling settings. The import block was used instead of the step input because the exact solar data was imported and that acts as a disturbance. The new Simulink block is shown below.

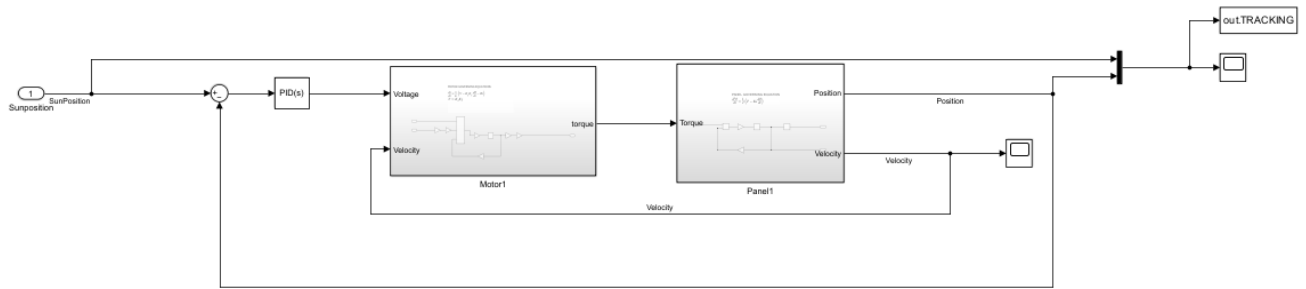


Figure 27: Simulink block diagram used for importing solar data.

It is seen from the plots above that the sun for both winter and summer rise and set at the same angle however they set at different times, the sun sets later in summer which is also shown in the plot. The plot further confirms reality in the sense that there are longer hours to the sun exposure in summer as opposed to winter, from this data we will be able to plot the position response of our controlled system to correctly observe its performance in tracking the sun.

5.1 Summer tracking

The system successfully tracks the sun, as it is seen in the figure below that there is no error between the position of the sun and the position of the solar tracker. This means that our controller can compensate for any errors in the process, and we have seen from the data discussed under the controller section in this report that our PID resulted in optimal response since the system is able to correct and reaches steady state within 0.256 seconds which is a quick time to correct for any errors.

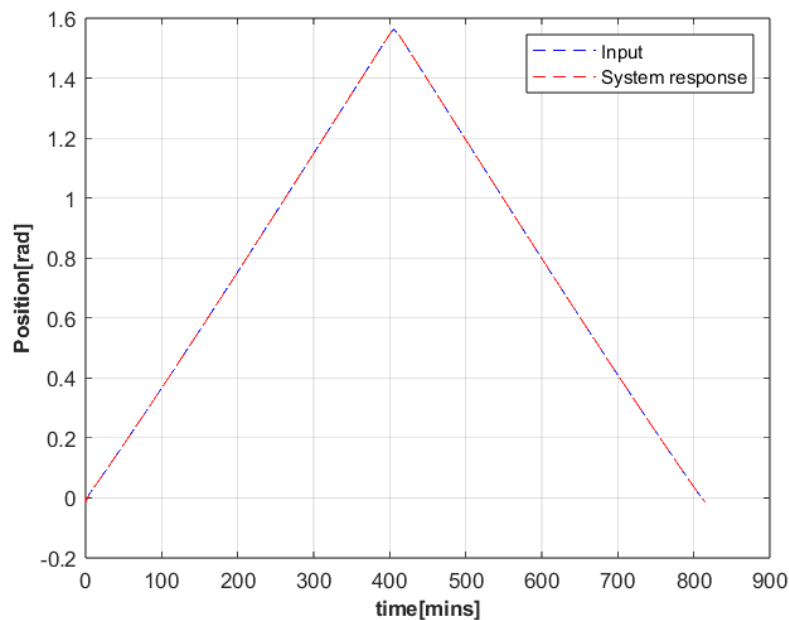


Figure 28: Summer solar tracking position vs time graph.

5.2 Winter tracking

The winter data applied for our controlled system also confirms the test we have performed for our summer data that the system is able to successfully track the position of the sun. This is due to the successful design of our PID controller as it enhances the performance of the system in terms of how fast it reaches steady state when introduced to a disturbance. However, at this point our system is not intelligent enough to return to its initial position when the sun has set hence further information is discussed in the instrumentation section which outlines the systems or components required to fully achieve the final state of an intelligent solar tracking system.

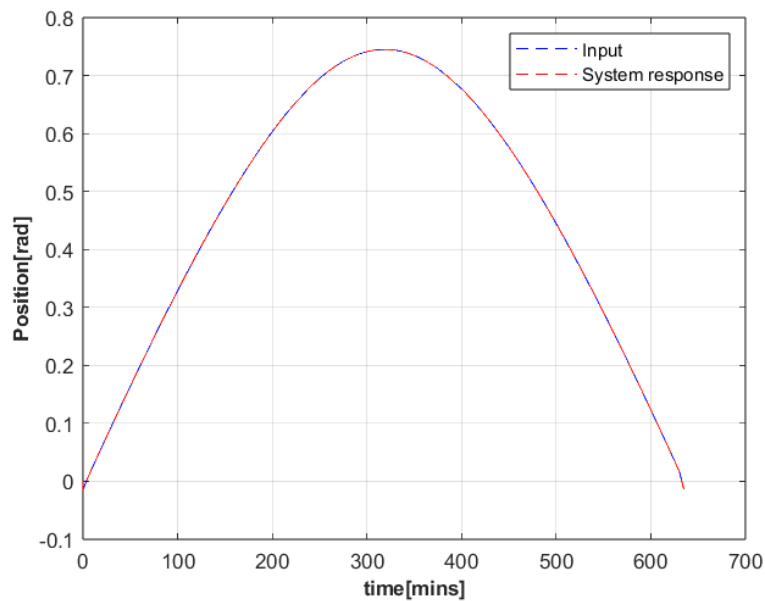


Figure 29: Winter solar tracking position vs time graph.

6 CONCLUSION

The controller design optimized the performance of the mechatronic system by ensuring stability, minimizing overshoot, improving response time, and eliminating steady-state error. The controller analyzed includes proportional, integral, and derivative components: the proportional controller provided immediate error correction, the integral controller addressed steady-state error, and the derivative controller improved the system's stability and reduced overshoot. Various controller types were evaluated, and it was found that the PI controller effectively matches the output to the reference input and eliminates steady-state error, although it introduces overshoot. The addition of derivative action in the PID controller further refined the system performance by reducing oscillations and improving settling time. Despite the complexities in tuning all three parameters, the PID controller achieved a smooth response with minimal overshoot, demonstrating significant improvements in system performance compared to both the uncontrolled system and the system with only proportional control.

The plots of the solar data indicated that while the sun rises and sets at the same angle in both seasons, it sets later in summer, reflecting longer daylight hours. The system successfully tracked the sun with no error between the solar position and the tracker, demonstrating the controller's ability to compensate for errors and achieve steady state within 0.256 seconds. Both winter and summer data confirmed the PID controller's effectiveness. However, the system currently lacks the capability to return to its initial position after sunset, which is discussed in the instrumentation section for future improvements.

In conclusion, the implementation of a PID-controlled solar tracking system was successful in optimizing solar panel alignment, significantly enhancing energy absorption in the Disteneng area. Given the ongoing load shedding in South Africa, reaching up to stage 8, traditional static axis systems have proven inadequate. The developed controller effectively tracked the sun's position with no error between the solar tracker and the sun, achieving rapid steady-state correction within 0.256 seconds. This improvement demonstrates the potential of the PID controller to enhance the efficiency and reliability of solar energy systems, addressing the urgent need for optimized energy solutions in regions affected by frequent power outages.

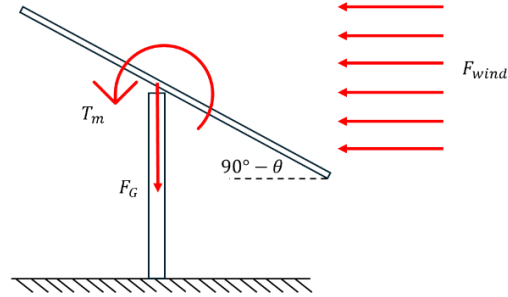
REFERENCES

- [1] “Statssa,” Department:Statistic South Africa Republic of South Africa, 5 July 2018. [Online]. Available: [https://www.statssa.gov.za/?p=11292#:~:text=South%20Africa%20is%20still%20largely,gas%20\(3%2C2%25\)..](https://www.statssa.gov.za/?p=11292#:~:text=South%20Africa%20is%20still%20largely,gas%20(3%2C2%25)..) [Accessed 4 04 2024].
- [2] J. Bohlmann and R. Inglesi-Lotz, “Examining the determinants of electricity demand by South African households per income level,” *Energy Policy*, vol. 148, p. 111901, 2021.
- [3] M. Wiese and L.-M. van der Westhuizen, “Impact of planned power outages (load shedding) on consumers in developing countries: Evidence from South Africa,” *Energy Policy*, vol. 187, p. 114033, 2024.
- [4] M. M. S. M. L. S. J. F. L. and R. , “Predicting Coal Consumption in South Africa Based on Linear (Metabolic Grey Model), Nonlinear (Non-Linear Grey Model), and Combined (Metabolic Grey Model-Autoregressive Integrated Moving Average Model) Models,” *Sustainability*, vol. 10, p. 2552, 07 2018.
- [5] “BusinessTechSA,” [Online]. Available: <https://businesstech.co.za/news/energy/630667/south-africas-horror-year-of-load-shedding-heres-how-it-compares/>. [Accessed 04 04 2024].
- [6] N. N. a. G. S. a. A. E. a. M. and J. , “Temperature and relative humidity trends in the northernmost region of South Africa, 1950–2016,” *South African Journal of Science*, 11 2021.
- [7] Mabunda and N. , “Use of Photovoltaic Energy to Minimize the Impact of Load-shedding in South Africa,” pp. 1-4, 2021.
- [8] “The Department of Planning, Monitoring and Evaluation and the National Department of Human Settlements undertook an Impact and Implementation Evaluation of,” [Online]. Available: <https://www.dpme.gov.za/publications/Reports%20and%20Other%20Information%20Products/DPME%20-%20Social%20Housing%20Programme%20-%20Combined.pdf>.
- [9] “Heavenly Rays | Electrical, Solar, Security and General Maintenance Services,” [Online]. Available: <https://heavenlyrays.co.za/>. [Accessed 04 04 2024].
- [10] HELIENE, 2017. [Online]. Available: <https://heliene.com/72-cell-monocrystalline-photovoltaic-module/>. [Accessed 07 04 2024].

- [11 ENF, “Solar Panel Directory,” [Online]. Available: <https://www.enfsolar.com/pv/panel>. [Accessed 04 04 2024].
- [12 A. Panday, “ULWAZI,” [Online]. Available: https://ulwazi.wits.ac.za/courses/55030/files/6563087?module_item_id=707988. [Accessed 08 May 2024].
- [13 “The PID Controller and Theory Explained,” EMERSON, 30 Mar 2023. [Online]. Available: <https://www.ni.com/en/shop/labview/pid-theory-explained.html>. [Accessed 17 May 2024].
- [14 “zybooks,” [Online]. Available: <https://learn.zybooks.com/zybook/ACMECN4029APandayWinter2024/chapter/7/section/2>. [Accessed 17 May 2024].
- [15 Sandeep D. Hanwate and Yogesh V. Hote, “Design of PID controller for sun tracker system using QRAWCP approach,” *International Journal of Computational Intelligence Systems*, vol. 11, no. DOI: 10.2991/ijcis.11.1.11, pp. 133-145, 2018.
- [16 sunearthtools, “sunearthtools,” [Online]. Available: https://www.sunearthtools.com/dp/tools/pos_sun.php#google_vignette. [Accessed 19 05 2024].

APPENDICES

Appendix A1: linearization of the mathematical model.



Sum of moment about the axis of rotation

$$J\ddot{\theta} = T - k_d\dot{\theta} - \frac{1}{2}C_D\rho v_\infty^2 lw \cos \theta$$

$$T = k_g k_t i$$

$$J = \frac{1}{12}m(l^2 \cos^2 \beta + d^2 \sin^2 \beta + w^2)$$

$$\beta = 90 - \theta$$

$$J = \frac{1}{12}m(l^2 \sin^2 \theta + d^2 \cos^2 \theta + w^2)$$

Substituting J and T in the main equation:

$$\frac{1}{12}m(l^2 \cos^2 \beta + d^2 \sin^2 \beta + w^2) \ddot{\theta} = k_g k_t i - k_d \dot{\theta} - \frac{1}{2}C_D \rho v_\infty^2 lw \cos \theta$$

$$\frac{1}{12}m(l^2 \sin^2 \theta + d^2 \cos^2 \theta + w^2) \ddot{\theta} = k_g k_t i - k_d \dot{\theta} - \frac{1}{2}C_D \rho v_\infty^2 lw \cos \theta$$

Linearization:

Let

$$f = -\frac{1}{12}m(l^2 \sin^2 \theta + d^2 \cos^2 \theta + w^2) \ddot{\theta} + k_g k_t i - k_d \dot{\theta} - \frac{1}{2}C_D \rho v_\infty^2 lw \cos \theta$$

$$f = f(\ddot{\theta}, \dot{\theta}, \theta, i)$$

Employing Taylor series:

$$f = \frac{df}{d\ddot{\theta}} \Delta \ddot{\theta} + \frac{df}{d\dot{\theta}} \Delta \dot{\theta} + \frac{df}{d\theta} \Delta \theta + \frac{df}{di} \Delta i + f_0$$

Initial conditions when $t=0$.

$$\ddot{\theta}_0 = \dot{\theta}_0 = \theta_0 = i_0 = 0$$

The f_0 term resulted to zero, and hence the linearized equation is presented below.

$$\frac{m}{12} (l^2 + w^2) \Delta \ddot{\theta} = k_g k_t \Delta i - k_d \Delta \dot{\theta}$$

Appendix A2: Root locus Analytical:

From the block diagram represented above, the characteristic equation of the open loop system is shown in the equation below:

$$G(s)H(s) = \frac{1}{0.00014s^3 + 0.070773s^2 + 100.15s} \quad (18)$$

The characteristic equation for the general problem is represented by equation (21):

$$1 + \frac{K}{0.00014s^3 + 0.070773s^2 + 100.15s} = 0 \quad (20)$$

The system has 3 of poles and does not have zeros, i.e., $P=3$ and $Z=0$, respectively.

Using Guides 2 and 3:

There are 3 poles located at $s_1 = 0$ and $s_{2,3} = -252.61 \pm 807.18i$. Therefore, this indicated that there will 3 loci starting at 0 and the other 2 starting at -252.61 ± 807.18 on the root locus. Since there are no zeros, all the loci will tend to infinity along the asymptote.

Guide 5:

The breakaway and break-in points were found from using $\frac{dK}{ds} = 0$, where:

$$K = 0.00014s^3 + 0.070773s^2 + 100.15s \quad (21)$$

$$\frac{dK}{ds} = 0.00042s^2 + 0.1415s + 100.15 \quad ()$$

The points were calculated to be at $s_{1,2} = -168.45 \pm 458.34i$ on the root locus. The corresponding value of K at the breakaway point was calculated to be ***

Guide 6:

Using the following equation, the angles that the two asymptotes make with the real axis were found to be at $\theta = -60^\circ, 60^\circ$ and -180°

$$\theta = \frac{n180^\circ}{P-Z} \quad ()$$

Guide 7:

The common point of intersection for the for the two loci were to be at ** using the below equation.

$$\sigma = \frac{\sum S_P - \sum S_Z}{P-Z} = 168.407 \quad ()$$

Guide 8

Calculations of the point at where the loci cross the imaginary plane were done by substituting $s = i\omega$ into the characteristic equation of K. From which we obtained:

$$\omega = 0, K = 0, \quad \text{or,} \quad \omega = 845.154, K = 50627.971.$$

